Helical magnetic structure of epitaxial films of nanolaminated Mn_2GaC MAX phase

J. Dey,[1] E. Jedryka,[1] R. Kalvig,[1] U. Wiedwald,[2] M. Farle,[2] J. Rosen,[3] and M. Wójcik[1]

[1]*Institute of Physics, Polish Academy of Sciences, Aleja Lotników 32/46, Warsaw PL-02668, Poland*

[2]*Faculty of Physics and Center for Nanointegration (CENIDE), University of Duisburg-Essen, Duisburg 47057, Germany*

[3]*Materials Design, Department of Physics, Chemistry and Biology (IFM), Linköping University, Linköping SE-58183, Sweden*

(Received 12 May 2023; accepted 20 July 2023; published 9 August 2023)

Nanolaminated Mn_2GaC epitaxial films crystallizing in the hexagonal structure belong to the family of MAX phase compounds and display complex magnetic interactions. While the critical temperature of the order-disorder transition is 507 K, at around 214 K this compound undergoes a first-order phase transition with the magnetic structure below the transition point not being fully resolved. Previous studies indicated a noncollinear spin arrangement, but a specific magnetic structure could not be defined. In this work we present the results of ^{69}Ga, ^{71}Ga, and ^{55}Mn NMR experiments performed at 4.2 K in an external in-plane magnetic field up to 1 T. The in-depth analysis of the experimental results shows a helical magnetic structure consisting of the ferromagnetically coupled Mn-C-Mn slabs that are twisted across the Ga layer by 167.2° with respect to the next Mn-C-Mn slab. As a result, the magnetic structure presents a spiral propagating along the out-of-plane direction (hexagonal *c* axis) with a pitch of around 14 lattice constants.

DOI: 10.1103/PhysRevB.108.054413

I. INTRODUCTION

Mn_2GaC heteroepitaxial films belong to the MAX phase family of compounds, being composed of nanolaminated carbides and nitrides and described as $M_{n+1}AX_n$, where M is a transition metal, A stands for an A-group element (mostly groups 13 and 14), X denotes carbon or nitrogen, and n can take the numbers 1, 2, or 3. A vigorous interest in materials from the MAX phase family has started with the breakthrough papers by Barsoum, showing that the $M_{n+1}AX_n$ ($n = 1$–3) compounds display a peculiar combination of ceramic and metallic properties such as high stiffness, oxidation resistance, machinability, and high damage tolerance [1,2]. These reports have spurred a lot of research interest in this family of compounds, consisting now of more than 155 phases [3]. It was found that the outstanding mechanical properties are due to a mixture of strong M-X bonds and weaker M-A bonds [4]. Further studies suggest that some of the MAX phases can display anisotropic electronic and thermal transport properties [5–7].

Adding magnetism as a new degree of freedom was a natural next target, especially since their naturally layered structure has a potential to achieve functionalities similar to, or even going beyond, those of the artificially prepared multilayers [8]. The first experimental observations of the magnetic MAX phases were reported in $Cr_{2-x}Mn_xGaC$ [9] and in the solid solution $(Cr_{0.75}Mn_{0.25})_2GeC$ [10]. Since then, the magnetic response has been reported in other Cr- and/or Mn-based bulk materials, eg., [11] and thin films, e.g., $(Cr_{0.5}Mn_{0.5})_2GaC$ [12], $(Mo_{0.5}Mn_{0.5})_2GaC$ [13]. Interestingly, all the bulk magnetic MAX phases reported to date featured a mixed composition of the M sublattice. It can thus be speculated that the lattice strain due to alloying plays a role in stabilizing the structure. The first magnetic MAX phase to contain a single M element was a Mn_2GaC thin film grown on the MgO(111) substrate [14]. Here the epitaxial tensile strain (around 2%) seems to be the stabilizing factor, since no Mn_2GaC phase has been reported in a bulk form. Bearing in mind the well-known effect of strain on the magnetic properties (e.g., [15]), it can be expected that the inherent strain in these films influences the magnetism. Indeed, the reported results of the density-functional theory (DFT) calculations, have shown that while the easy axis in Mn_2GaC is always parallel to the atomic planes, different spin configurations can be achieved through the strain engineering [16]. The strain related to a choice of substrate or applied pressure may be used to tune the magnetic properties, such as the magnetocrystalline anisotropy energy (MAE) [16].

Mn_2GaC crystallizes in the hexagonal structure (space group $P6_3/mmc$) and presents a nanolaminated stack of ferromagnetically coupled Mn-C-Mn blocks interleaved with the atomic layers of gallium, piled along the hexagonal c axis as shown in Fig. 1.

The DFT calculations performed for Mn_2GaC predict that the exchange interaction between the Mn layers varies along the out-of-plane axis: it is always ferromagnetic for the Mn-C-Mn slab but in the case of the Mn-Ga-Mn it shows a strong dependence on the Mn-Ga interatomic distance, changing from ferromagnetic to antiferromagnetic with the increasing distance [18]. Therefore the ferromagnetic (FM) Mn-C-Mn slabs can be treated as a single spin moment (a "supermoment"), whereas several antiferromagnetic (AFM) structures across the Ga layer can be proposed, characterized by almost the same energy minima [18]. As a result, the ground state of Mn_2GaC can be strongly degenerated into the FM and AFM states and sensitively depends on temperature, strain, and magnetic field [19]. The critical temperature of the order-disorder transition in Mn_2GaC is 507 K. At around 214 K this compound undergoes a first-order phase transition [19], but the magnetic structure below the transition point

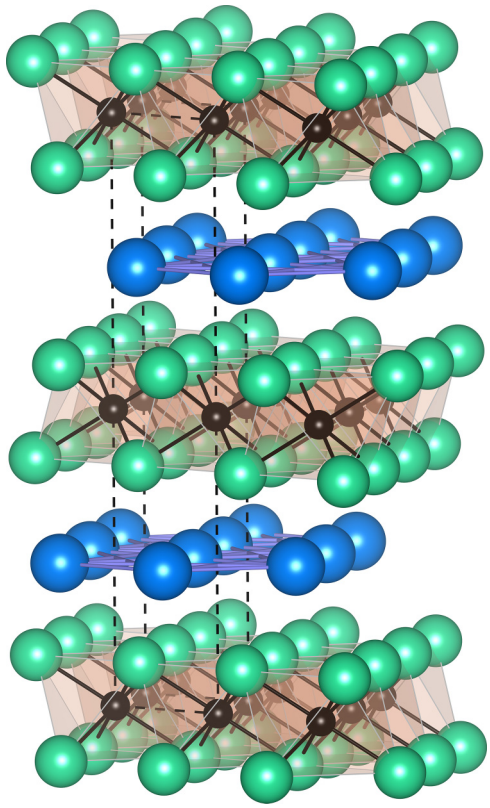

FIG. 1. Hexagonal layered structure of Mn_2GaC film (MAX phase): Mn, green; Ga, blue; and C, black. Salmon-shaded area indicates the layers forming a single "supermoment," as discussed in the text. Black dashed lines delineate the unit crystal cell. This drawing was prepared using the VESTA software [17].

is not yet clear and different low-energy antiferromagnetic configurations have been proposed from theoretical considerations [16,18]. However, the hitherto experimental studies do not prove any of these structures, while excluding the others. The experiments of unpolarized neutron reflectometry have shown the features of antiferromagnetic order with periodicity of two unit cells [20], which would correspond to the AFM$[0001]^A_4$, one of the collinear antiferromagnetic structures deduced from the theoretical (DFT) calculations. In this scenario the two subsequent supermoments form a ferromagnetic cluster consisting of the four manganese and two carbon layers while the consecutive clusters along the c axis are coupled antiferromagnetically, so that the net magnetic moment cancels out. This is, however, at odds with the reported magnetization measurements showing at low temperatures a nonzero remanent magnetization [18,21]. Our preliminary zero-field NMR investigations carried out on ^{69}Ga, ^{71}Ga, and ^{55}Mn nuclei suggested a noncollinear arrangement of manganese supermoments across a gallium layer [22]. However, the specific low-temperature magnetic structure in this material could not be proposed based on the zero-field NMR experiments alone. In this work we present new ^{69}Ga, ^{71}Ga, and ^{55}Mn NMR data, taken in the presence of the external in-plane magnetic field, that have made it possible to unambiguously identify the specific magnetic structure. The presence of a helical spiral of the Mn magnetic moments propagating along the film normal (the hexagonal c axis of the material) has been demonstrated and the helix parameters have been determined.

II. EXPERIMENT

The experiments have been performed on a 100-nm $Mn_2GaC(0001)/MgO(111)$ film, deposited by magnetron sputter epitaxy using three confocal sources with elemental targets: manganese (99.99% purity), gallium (99.99995% purity), and carbon (99.99% purity). Due to the low melting temperature of Ga, that target was kept in a stainless-steel crucible positioned directly under the substrate. The substrate was cleaned in an ultrasonic bath of acetone, ethanol, and isopropanol for 10 min and then kept at the deposition temperature of 550° for 60 min prior to deposition. The current applied to the targets was regulated and the sputtering rates of Mn and C were calibrated to give a 2:1 ratio. Further information regarding the cosputtering including a liquid Ga target can be found in Ref. [23].

NMR signals were observed in the range 130–300 MHz and recorded with 0.5 MHz steps at $T = 4.2$ K using a phase-sensitive NMR spin-echo spectrometer [24]. The data were taken according to the Panissod protocol [25] to ensure a correct signal intensity at each frequency, irrespective of the variation of the NMR enhancement factor. Several NMR spectra have been recorded, applying the in-plane external magnetic field in the range from 0 to 1 T. The external magnetic field adds to the internal field on site of nucleus and the NMR frequency ν is given by the expression [26]

$$\nu = \gamma|\vec{B}_{\rm eff}| \approx \gamma|\vec{B}_{hf} + \vec{B}_{\rm ext}|, \tag{1}$$

where γ denotes the nuclear gyromagnetic ratio and $\vec{B}_{\rm eff}$ is the effective magnetic field, consisting of the external field $\vec{B}_{\rm ext}$ and the hyperfine field $\vec{B}_{hf}$ generated at the nucleus by the surrounding electrons and magnetic dipoles. A full description of all contributions to the internal magnetic fields on nucleus and their manifestation in the NMR spectra can be found in Ref. [26]. For the sake of the present investigation we recall here that the main contribution to the hyperfine field comes from the contact Fermi term $\vec{B}^{cF}_{hf}$ generated by the on-site magnetic moment of a studied nucleus ($\vec{\mu}_{\rm loc}$) and by the magnetic moments of the nearest neighbors ($\sum \vec{\mu}_i$)

$$\vec{B}^{cF}_{hf} = \widehat{A}\vec{\mu}_{\rm loc} + \sum_{i=1}^{n} \widehat{A}_{\rm trans}\vec{\mu}_i, \tag{2}$$

where $\widehat{A}$ is the on-site hyperfine interaction constant and $\widehat{A}_{\rm trans}$ describes the hyperfine field transferred from the nearest magnetic neighbors.

III. RESULTS AND DISCUSSION

Structural analysis based on x-ray diffraction (XRD) and reflection (details provided in [14]) shows epitaxial growth of Mn_2GaC, with minute traces of the antiperovskite Mn_3GaC. The epitaxial relationship for the Mn_2GaC film grown onto the MgO(111) surface is $[1\,1\,\bar{2}\,0]Mn_2GaC \parallel [1\,0\,\bar{1}]MgO$ in the film plane and $(0001)Mn_2GaC \parallel (111)MgO$ out of the plane. The calculated a and c parameters obtained from XRD

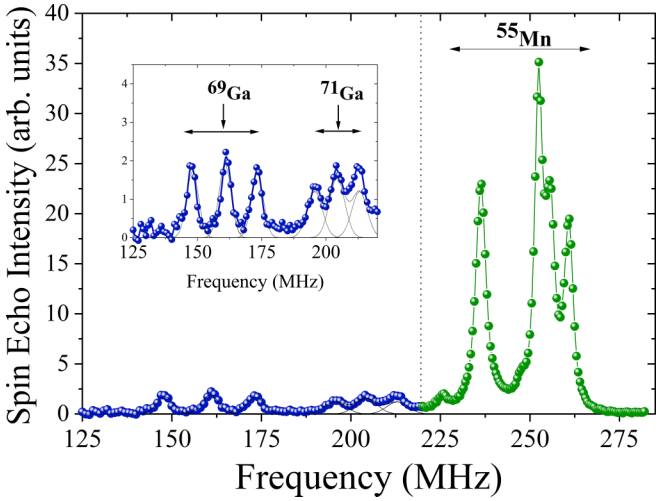

FIG. 2. Zero-field NMR spectra of ^{69,71}Ga and ^{55}Mn nuclei recorded at 4.2 K from a $Mn_2GaC(0001)/MgO(111)$ film. The resonance frequencies are determined by the respective hyperfine fields due to manganese magnetic moments (transferred hyperfine field in the case of nonmagnetic gallium). Figure reprinted with the editor's permission from Ref. [22].

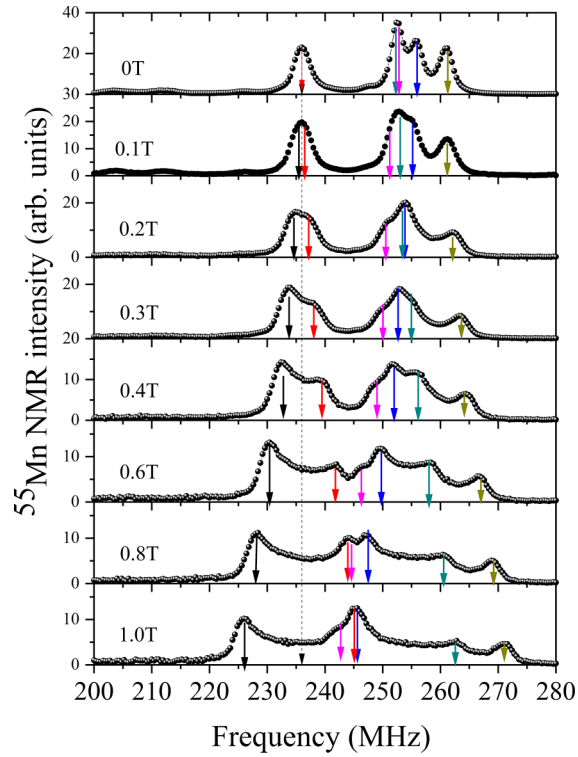

FIG. 3. ^{55}Mn NMR spectra recorded from $Mn_2GaC(0001)/MgO(111)$ film in the presence of the in-plane external magnetic field, ranging from 0 to 1.0 T. Colored arrows indicate the characteristic features (peaks) in the subsequent spectra.

are 2.90 and 12.55 Å, respectively. Compositional analysis based on energy dispersive x-ray analysis (EDX) shows a relative composition of 52 at. % Mn, 23 at. % Ga, and 23 at. % C, which, within the error bars, corresponds to the ideal stoichiometry (details provided in [14]), though it should be noted that EDX cannot be used for accurate quantification of light elements (such as C). Further characterization, using the cross-sectional high-angle annular dark-field scanning transmission electron microscopy (HAADF/STEM) has shown a high-quality, atomically layered structure, where the Ga atomic layers alternate with a set of two Mn layers. The high crystal quality and structure of the sample was independently confirmed by the selected area electron diffraction pattern [19].

Figure 2 presents the zero-field NMR spectrum recorded at 4.2 K from the $Mn_2GaC(0001)/MgO(111)$ epitaxial film. This spectrum has been extensively discussed in our previous paper [22]. According to Eq. (1), the low-intensity resonances in the range 140–220 MHz are unambiguously assigned to the two gallium isotopes, ^{69}Ga ($\gamma = 10.22$ MHz/T) and ^{71}Ga ($\gamma = 12.98$ MHz/T), whereas the structure in the range 220–270 MHz is assigned to ^{55}Mn NMR ($\gamma = 10.5$ MHz/T). In the case of ^{55}Mn nuclei, the main contribution to the hyperfine field is due to the on-site manganese magnetic moment, whereas in the case of a nonmagnetic gallium the only source of hyperfine field at Ga nuclei consists of the transferred field from the surrounding Mn magnetic moments [second part of Eq. (2)]. The characteristic triplet structure of the gallium resonances is readily understood as being due to the interaction of the Ga nuclear quadrupole moment (the nuclear spin moment of ^{69,71}Ga : $I = 3/2$) with the electric field gradient present at the site of the nucleus. Such clearly resolved quadrupolar structure is evidence of a perfect symmetry of the charges surrounding the nucleus and thus confirms a good crystalline quality of the studied sample.

In a crystal of high quality, considering that all Mn atoms are crystallographically equivalent in the hexagonal structure of Mn_2GaC, one would expect a single resonance line in the ^{55}Mn NMR spectrum, possibly with a five-component quadrupolar structure (the nuclear spin moment of ^{55}Mn: $I = 5/2$). However, the irregular shape of the NMR spectrum recorded in the range 220–270 MHz cannot be attributed to the quadrupolar structure, and rather shows that amongst the crystallographically equivalent Mn positions there are some magnetically inequivalent Mn sites. To shed more light on the complex ^{55}Mn NMR spectrum, additional experiments have been performed, applying an in-plane external magnetic field. The respective ^{55}Mn NMR spectra, recorded at different external field values, are presented in Fig. 3.

Clearly, the in-field spectra cover a progressively broader frequency span and reveal an even more complex structure. To facilitate the analysis, the characteristic spectral features (peaks) have been marked in Fig. 3 with arrows of different colors, and their position as a function of the magnetic field strength is shown in Fig. 4(a).

This chart is very suggestive and demonstrates that the observed multiple peaks can be grouped into three bifurcated NMR lines, with all the frequency branches linearly increasing/decreasing with a slope equal to the Mn gyromagnetic ratio, $\gamma = 10.5$ MHz/T. We also note that while the two high-frequency lines overlap, the line at lowest frequency is well separated and its evolution can be followed all the way up to the field of 1 T. In view of the identical in-field behavior, it can be assumed that the remaining components of the NMR

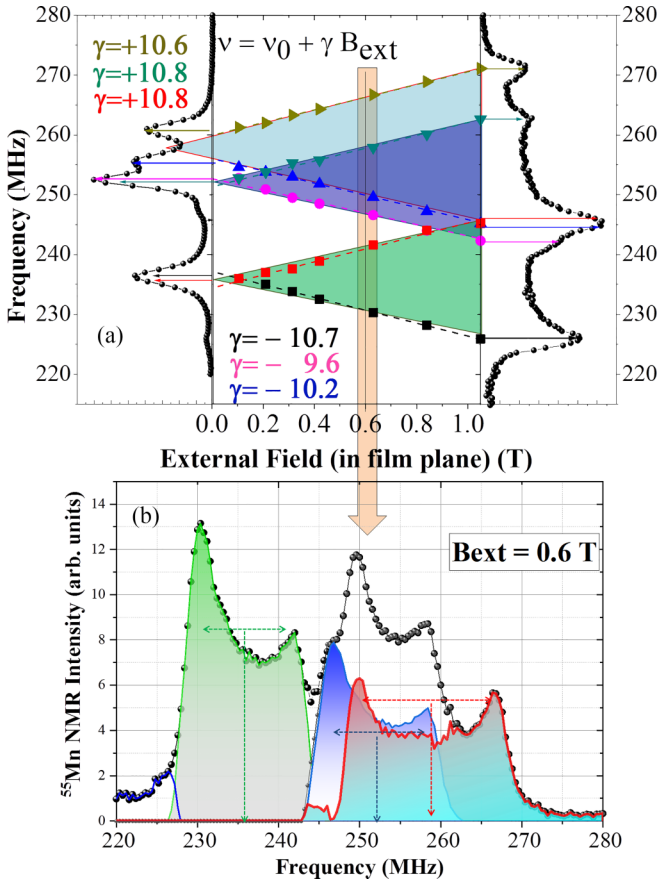

FIG. 4. (a) Frequency position of the characteristic peaks in the ^{55}Mn NMR spectra from $Mn_2GaC(0001)/MgO(111)$ film vs the in-plane external field strength. (b) Decomposition of the ^{55}Mn NMR spectrum recorded at $B_{ext} = 0.6$ T into three components taking as a reference the intensity distribution of the well-resolved low-frequency line (230–242 MHz).

spectrum have a similar shape, mimicking the well-resolved low-frequency line. Therefore, we have tentatively disentangled the ^{55}Mn NMR spectrum recorded at 0.6 T using the pattern of the low-frequency line shape, as shown in Fig. 4(b). This line shape can be easily explained considering that the NMR frequency probes the orientation of the local field B_{hf} (i.e., the orientation of the on-site magnetic moment μ_{loc}) relative to that of the external magnetic field, therefore Eq. (1) can be expressed as

$$\nu = \gamma|\vec{B}_{hf} + \vec{B}_{ext}| = \gamma[B_{hf} - B_{ext}\cos(\varphi)]. \quad (3)$$

In a sample with varying orientation of the local magnetic moments, each forming a different angle φ with the direction of the external field, the NMR signals cover the frequency range spanning between the frequencies of the two extreme orientations. It has been shown [27] that in such case the NMR signal intensity can be expressed as a function of frequency ν by

$$I(\nu) = \int_{\varphi_1}^{\varphi_2} D[\nu(\varphi)] f[\nu - \nu(\varphi)] d\varphi, \quad (4)$$

where $f[\nu - \nu(\varphi)]$ is a local line shape (assumed Gaussian) and $D[\nu(\varphi)]$ is the intensity of the NMR signal from a given

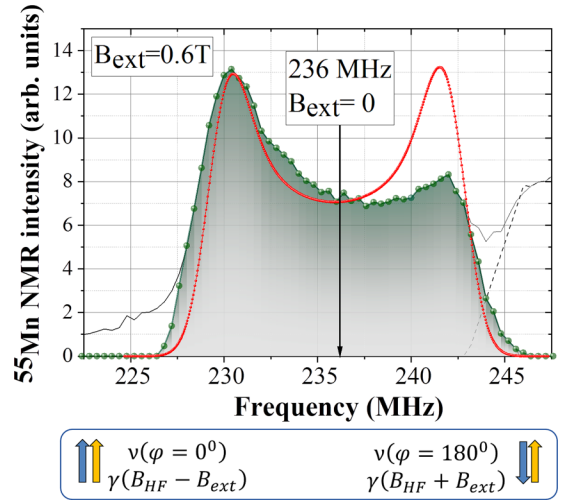

FIG. 5. Black solid line: intensity distribution of the NMR signal computed using Eqs. (4) and (5) for the case of $B_{ext} = 0.6$ T, assuming a continuous variation of the angle φ between 0° and 180°. Green shaded area: the corresponding part of the experimental ^{55}Mn NMR spectrum. The arrow at 236 MHz indicates the position of the NMR line at zero external field.

spin making an angle with the direction of the external magnetic field (φ spanning the range from φ_1 to φ_2), and can be expressed as [28]

$$D[\nu(\varphi)] = \frac{dN}{d\nu} \approx k\left(\frac{d\nu}{d\varphi}\right)^{-1} = k\frac{1}{\sin\varphi}. \quad (5)$$

The function $[\sin(\varphi)]^{-1}$ diverges at $\varphi = 0°$ and $\varphi = 180°$, so the most densely populated states are those with parallel and antiparallel orientation of the magnetic moments with respect to the external field direction. Using Eqs. (4) and (5) we have computed a model NMR spectrum for the case of $B_{ext} = 0.6$ T and the angle φ varying continuously between 0° and 180°.

Figure 5 presents the comparison of this computed symmetrical spectrum and the experimental one showing that this intensity distribution reproduces the main features of the experimental NMR spectrum. The asymmetry of the experimental spectrum reflects the preferred orientation of spins along the external magnetic field. Since the hyperfine field is directed opposite to the magnetic moment, the population of spins contributing to the low-frequency end of the NMR spectrum is enhanced. In view of Eq. (3) such a broad distribution of spin orientations means that a bunch of identical magnetic moments contributing at zero field to a single NMR line at 236 MHz become distinguishable in the presence of an in-plane external field because they receive a different, angular-dependent component of the external magnetic field.

To visualize this effect, we have transformed this segment of the experimental NMR spectrum from the frequency domain into the "angle domain," as shown in Fig. 6(a). Bearing in mind that the Mn-C-Mn trilayer is magnetically equivalent to a single layer defined as supermoment," this analysis unequivocally shows that the orientation of the individual supermoments in Mn_2GaC sweeps all possible angles φ between parallel and antiparallel orientations with respect to the external field.

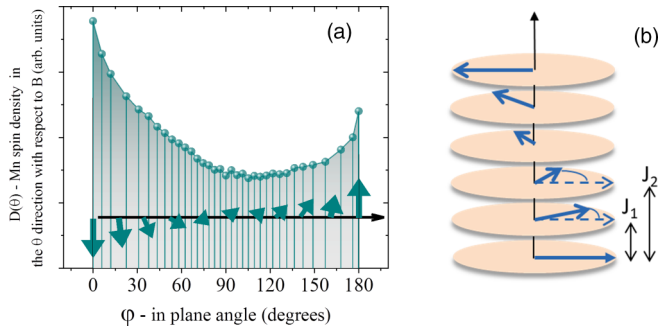

FIG. 6. (a) Diagram of manganese spin density as a function of orientation with respect to the in-plane field direction determined from the ^{55}Mn NMR spectrum at 0.6 T. (b) Schematic representation of the spin spiral involving subsequent ferromagnetically coupled Mn-C-Mn layers represented by a single supermoment. J_1 (> 0) and J_2 (< 0) denote the exchange interaction between the respective supermoments.

This spread of orientations is additionally confirmed by the in-field NMR experiments on gallium. Figure 7(a) shows the ^{69}Ga NMR spectra recorded at several values of the external in-plane magnetic field. With increasing field strength the frequency span of all three components of the ^{69}Ga triplet NMR line gets expanded. Similar to the case of ^{55}Mn NMR the population of spins contributing to the signal at the low-frequency end of this span is enhanced, showing that the transferred hyperfine field on Ga is oriented opposite to the Mn magnetic moment.

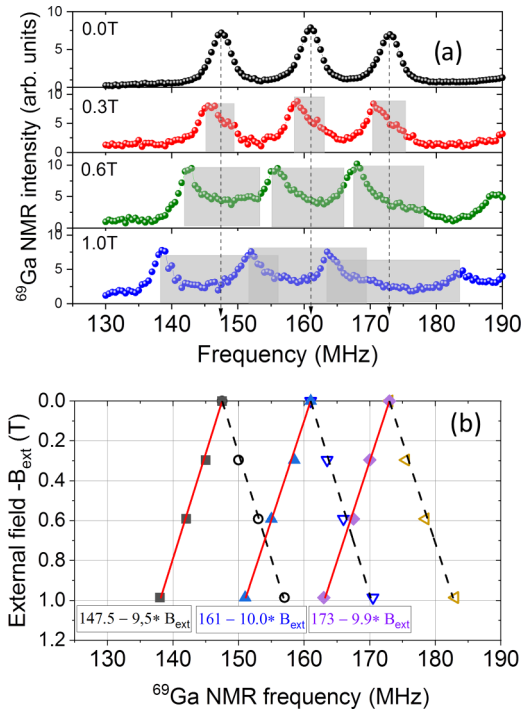

FIG. 7. (a) ^{69}Ga NMR spectrum (quadrupolar-split triplet line) recorded at 0, 0.3, 0.6, and 1 T of the external in-plane magnetic field. The dotted lines indicate the zero-field position of the respective triplet components whereas shaded areas mark their extent at a given value of the external field. (b) Frequency position of the characteristic peaks in the ^{69}Ga NMR spectra from $Mn_2GaC(0001)/MgO(111)$ film vs the in-plane external field strength.

The position of the extreme frequencies (less pronounced on the high-frequency end) is plotted in Fig. 7(b), showing that the frequency shift follows a slope close to the gyromagnetic ratio of ^{69}Ga nuclei (10.2 MHz/T). Bearing in mind that the only source of hyperfine field at gallium nuclei consists of the transferred field from the surrounding magnetic moments of manganese [cf. Eq. (2)], the in-field ^{69}Ga NMR spectra simply reflect the distribution of magnetic moments around them, providing another probe of their configuration, in addition to the direct observation via the ^{55}Mn NMR data.

Here, the question arises what kind of magnetic structure is responsible for the observed distribution of the magnetic moments. Considering the layered crystal structure of our MAX phase material the most straightforward suggestion would be a spin spiral propagating along the film normal (i.e., the hexagonal c axis), as shown in Fig. 6(b). In other words, the spin structure of the Mn_2GaC film can be envisaged as a helical stack of such supermoments interleaved by Ga layers and rotated in plane by a certain angle $\Delta\Phi$ with respect to the neighboring supermoment.

A helical spin order has been observed in a number of magnetic systems with a layered crystal structure. A well-established mechanism responsible for helimagnetism is the competition between the antisymmetric Dzyaloshinskii-Moriya interaction (DMI) and the FM interaction. This takes place when the inversion symmetry is broken at the thin-film interface or in the volume of a noncentrosymmetric material. A well-known group of the bulk materials displaying this property are the B20 transition metal monosilicides and monogermanides such as FeGe [29], MnSi [30], and $Fe_xCo_{1-x}Si$ [31,32]. On the other hand, the helical spin arrangement has been also observed in materials with the inversion symmetry, such as $EuNi_2As_2$ [33,34] and $EuCo_2P_2$ [35,36] with the $ThCr_2Si_2$ type structure. In this case, the helical structure is generated by the competing exchange interactions between the first nearest neighbor (J_1) and the second nearest neighbors (J_2) [see Fig. 6(b)]. It has been shown that to create a spin spiral, a following relation should be fulfilled: $J_2 < 0$ (antiferromagnetic) and $|J_1| < |4J_2|$ [37]. As a layered, centrosymmetric material Mn_2GaC belongs to this second case and the above criteria for the presence of helical state applied to the case of Mn_2GaC would require an antiferromagnetic J_2 exchange interaction between every second supermoment layer. And indeed, the Monte Carlo calculations of the exchange interactions performed up to the fourth nearest neighbors, have found J_2 negative (antiferromagnetic) in the considered unit-cell volume [16,18]. Moreover, the calculated value of J_1 also satisfies the above criteria of a spin spiral [16,18]. These calculations fully support the helical magnetic structure of the Mn_2GaC MAX phase thin film inferred from our analysis of the ^{55}Mn NMR spectra. Here we report a helical magnetic structure involving a block of the ferromagnetically coupled supermoments (Mn-C-Mn), rather than single atomic layers as was the case of the previously discussed noncentrosymmetric and centrosymmetric layered materials.

To estimate the spiral period let us consider the nearest neighborhood of Ga consisting of six Mn atoms. As shown

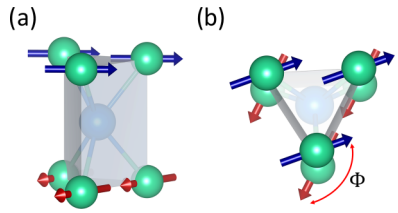

FIG. 8. Configuration of the nearest Mn neighbors (green balls) around a Ga atom (in the center of a trigonal prism). (a) Side view. (b) Top view. Blue and red arrows show the direction of magnetic moments in the consecutive Mn atomic planes. This drawing was prepared using the VESTA software [17].

in Fig. 8, they form a trigonal prism: three Mn atoms are located in the plane above the Ga atom and three below. In the scenario based on the DFT calculations, the Mn magnetic moments within the respective plane are strongly coupled together and belong to the two subsequent supermoments. Defining their orientation in the upper plane as the "x axis," the magnetic moments in the bottom plane are rotated by $\Delta\Phi$ with respect to x. Each of the six magnetic nearest neighbors provides the transferred hyperfine field, giving rise to the NMR spectrum observed on the ^{69}Ga and ^{71}Ga nuclei. Taking into account a local symmetry of Ga in the Mn_2GaC lattice, from the geometry of magnetic moment configuration one can show [38] that the cumulative hyperfine field transferred by the six Mn neighbors is given by the following expression:

$$\vec{B}_{\text{trans}} = 3\langle\vec{\mu}_{\text{Mn}}\rangle A_{\text{trans}}\sqrt{2+2\cos(\Phi)}. \tag{6}$$

From our ^{69,71}Ga NMR experiment the value of the transferred hyperfine field on Ga has been determined at 15.75 T and the average Mn magnetic moment $\langle\mu_{\text{Mn}}\rangle$ is found to be 2 μ_B [22]. Taking the transferred hyperfine interaction constant as $A_{\text{trans}} = 12$ T/μ_B [39], we obtain that the spin rotation between two subsequent supermoment layers is $\Phi = 167.2^\circ$ and twice this value (334.4°) over the lattice c parameter. This means that the pitch of a helix is incommensurate with the lattice constant and the first integer multiple of 360° will be reached only after 28 rotations, i.e., over 14 lattice distances. Bearing in mind that the crystal lattice parameter of Mn_2GaC is $c = 1.255$ nm, the full turn of a spiral is reached over the distance of 17.5 nm, giving almost six full turns of a spiral over the investigated film thickness (100 nm), and explaining the vast spread of spin directions observed in our experiments.

The origin of the high-frequency (> 240 MHz) part of the NMR spectrum is not clear. As shown above, it consists of the two overlapping Mn signals having the same features as the low-frequency part discussed in the previous paragraphs. A possible explanation is that some of the slightly misoriented crystal grains introduce the minuscule strain distribution and, consequently, different anisotropic orbital contribution to the ^{55}Mn hyperfine field, even if their magnetic moment and thus the contact Fermi contribution remain the same. Indeed, a strong magnetocrystalline anisotropy with (0001) as the easy planes, has been recently confirmed experimentally in the nanolaminated Mn_2GaC films with a single (0 0 0 1) or a mixed (0 0 0 1) and (1 0 $\bar{1}$ 3) orientation [21].

IV. CONCLUSIONS

In conclusion, the present NMR experiments indicate a spiral arrangement at 4.2 K of the magnetic Mn-C-Mn supermoments within a nanolaminated Mn_2GaC MAX phase film. The application of an external in-plane magnetic field made it possible to demonstrate the presence of a helix with a propagation vector extending along the hexagonal c axis (i.e., along the film normal). A pitch of a helix is incommensurate with the lattice parameter and has been estimated at around 14 lattice constants. These findings are fully consistent with the published results of Monte Carlo calculations performed for this compound, which predict ferromagnetic exchange interaction (J_1) between the first nearest neighbors, and antiferromagnetic exchange interaction (J_2) between every second supermoment layer [16,18]. In view of this, the nanolaminated Mn_2GaC films fulfill at low temperature the criteria necessary for the formation of a helical structure, providing strong theoretical support for the conclusions drawn from the present investigation.

ACKNOWLEDGMENTS

This work was supported by the National Science Center, Poland (Grant No. UMO-2019/35/B/ST3/03676). J.R. acknowledges support from the Swedish Research Council (2019-04233) and the Göran Gustafsson Foundation for Research in Natural Sciences and Medicine. U.W. and M.F. acknowledge support by the Deutsche Forschungsgemeinschaft (405553726) within CRC/TRR 270, projects B02 and A04.

[1] M. W. Barsoum, *MAX Phases: Properties of Machinable Ternary Carbides and Nitrides* (Wiley-VCH, Weinheim, Germany, 2013).

[2] M. W. Barsoum, The $M_{N+1}AX_N$ phases: A new class of solids: Thermodynamically stable nanolaminates, Prog. Solid State Chem. **28**, 201 (2000).

[3] M. Sokol, V. Natu, S. Kota, and M. W. Barsoum, On the chemical diversity of the MAX phases, Trends Chem. **1**, 210 (2019).

[4] M. Magnuson and M. Mattesini, Chemical bonding and electronic-structure in MAX phases as viewed by x-ray spectroscopy and density functional theory, Thin Solid Films **621**, 108 (2017).

[5] J. Rosen, M. Dahlqvist, S. I. Simak, D. R. McKenzie, and M. M. M. Bilek, Oxygen incorporation in Ti_2AlC: Tuning of anisotropic conductivity, Appl. Phys. Lett. **97**, 073103 (2010).

[6] T. Flatten, F. Matthes, A. Petruhins, R. Salikhov, U. Wiedwald, M. Farle, J. Rosen, D. E. Bürgler, and C. M. Schneider, Direct measurement of anisotropic conductivity in a nanolaminated $(Mn_{0.5}Cr_{0.5})_2GaC$ thin film, Appl. Phys. Lett. **115**, 094101 (2019).

[7] A. Champagne, J. L. Battaglia, T. Ouisse, F. Ricci, A. Kusiak, C. Pradere, V. Natu, A. Dewandre, M. J. Verstraete, M. W. Barsoum *et al.*, Heat capacity and anisotropic thermal conductivity in Cr_2AlC single crystals at high temperature, J. Phys. Chem. C **124**, 24017 (2020).

[8] A. S. Ingason, M. Dahlqvist, and J. Rosén, Magnetic MAX phases from theory and experiments: A review, J. Phys.: Condens. Matter **28**, 433003 (2016).

[9] S. Lin, P. Tong, B. Wang, Y. Huang, W. Lu, D. Shao, B. Zhao, W. Song, and Y. Sun, Magnetic and electrical/thermal transport properties of Mn-doped $M_{n+1}AX_n$ phase compounds $Cr_{2-x}Mn_xGaC$ ($0 \leqslant x \leqslant 1$), J. Appl. Phys. **113**, 053502 (2013).

[10] A. S. Ingason, A. Mockute, M. Dahlqvist, F. Magnus, S. Olafsson, U. B. Arnalds, B. Alling, I. A. Abrikosov, B. Hjörvarsson, P. O. Å. Persson *et al.*, Magnetic Self-Organized Atomic Laminate from First Principles and Thin Film Synthesis, Phys. Rev. Lett. **110**, 195502 (2013).

[11] A. Mockute, P. O. Å. Persson, F. Magnus, A. S. Ingason, S. Olafsson, L. Hultman, and J. Rosen, Synthesis and characterization of arc deposited magnetic $(Cr, Mn)_2AlC$ MAX phase films, Phys. Status Solidi RRL **8**, 420 (2014).

[12] A. Petruhins, A. S. Ingason, J. Lu, F. Magnus, S. Olafsson, and J. Rosen, Synthesis and characterization of magnetic $(Cr_{0.5}Mn_{0.5})_2GaC$ thin films, J. Mater. Sci. **50**, 4495 (2015).

[13] R. Meshkian, A. S. Ingason, U. Arnalds, F. Magnus, J. Lu, and J. Rosén, A magnetic atomic laminate from thin film synthesis: $(Mo_{0.5}Mn_{0.5})_2GaC$, APL Mater. **3**, 076102 (2015).

[14] A. S. Ingason, A. Petruhins, M. Dahlqvist, F. Magnus, A. Mockute, B. Alling, L. Hultman, I. Abrikosov, P. O. Å. Persson, and J. Rosen, A nanolaminated magnetic phase: Mn_2GaC, Mater. Res. Lett. **2**, 89 (2014).

[15] L. Cabral, F. H. Aragón, L. Villegas-Lelovsky, M. P. Lima, W. A. Macedo, and J. L. Da Silva, Tuning the magnetic properties of FeCo thin films through the magnetoelastic effect induced by the Au underlayer thickness, ACS Appl. Mater. Interfaces **11**, 1529 (2019).

[16] M. Dahlqvist and J. Rosen, Impact of strain, pressure, and electron correlation on magnetism and crystal structure of Mn_2GaC from first-principles, Sci. Rep. **10**, 11384 (2020).

[17] K. Momma and F. Izumi, VESTA 3 for three-dimensional visualization of crystal, volumetric and morphology data, J. Appl. Crystallogr. **44**, 1272 (2011).

[18] M. Dahlqvist, A. S. Ingason, B. Alling, F. Magnus, A. Thore, A. Petruhins, A. Mockuté, U. B. Arnalds, M. Sahlberg, B. Hjörvarsson, I. A. Abrikosov, and J. Rosen, Magnetically driven anisotropic structural changes in the atomic laminate Mn_2GaC, Phys. Rev. B **93**, 014410 (2016).

[19] I. P. Novoselova, A. Petruhins, U. Wiedwald, Á. S. Ingason, T. Hase, F. Magnus, V. Kapaklis, J. Palisaitis, M. Spasova, M. Farle *et al.*, Large uniaxial magnetostriction with sign inversion at the first order phase transition in the nanolaminated Mn_2GaC MAX phase, Sci. Rep. **8**, 2637 (2018).

[20] A. S. Ingason, G. K. Pálsson, M. Dahlqvist, and J. Rosén, Long-range antiferromagnetic order in epitaxial Mn_2GaC thin films from neutron reflectometry, Phys. Rev. B **94**, 024416 (2016).

[21] E. B. Thorsteinsson, A. S. Ingason, and F. Magnus, Magnetic ordering and magnetocrystalline anisotropy in epitaxial Mn_2GaC MAX phase thin films, Phys. Rev. Mater. **7**, 034409 (2023).

[22] J. Dey, M. Wójcik, E. Jedryka, R. Kalvig, U. Wiedwald, R. Salikhov, M. Farle, and J. Rosén, Non-collinear magnetic structure of the MAX phase Mn_2GaC epitaxial films inferred from zero-field NMR study (CE-5: L05), Ceram. Int. **49**, 24235 (2023).

[23] A. Petruhins, A. S. Ingason, M. Dahlqvist, A. Mockute, M. Junaid, J. Birch, J. Lu, L. Hultman, P. O. Å. Persson, and J. Rosen, Phase stability of $Cr_{n+1}GaC_n$ MAX phases from first principles and Cr_2GaC thin-film synthesis using magnetron sputtering from elemental targets, Phys. Status Solidi RRL **7**, 971 (2013).

[24] S. Nadolski, M. Wójcik, E. Jedryka, and K. Nesteruk, Automated pulsed NMR spectrometer for modern magnetic materials, J. Magn. Magn. Mater. **140-144**, 2187 (1995).

[25] P. Panissod, M. Malinowska, E. Jedryka, M. Wójcik, S. Nadolski, M. Knobel, and J. E. Schmidt, Inhomogeneous structure and magnetic properties of granular $Co_{10}Cu_{90}$ alloys, Phys. Rev. B **63**, 014408 (2000).

[26] E. Jedryka and M. Wójcik, *Nuclear Magnetic Resonance in Nanomagnetic Systems, in Nanomagnetic Materials, Fabrication, Characterization and Applications*, edited by A. Yamaguchi, A. Hirohata, and B. J. Stadler (Elseiver, New York, 2021).

[27] G. A. Murray and W. Marshall, A new interpretation of nuclear magnetic resonance in dilute ferromagnetic alloys, Proc. Phys. Soc. **86**, 315 (1965).

[28] P. Panissod, M. Wójcik, and E. Jedryka, *Supermagnets, Hard Magnetic Materials, Series C: Mathematical and Physical Sciences* (Kluwer Academic, Dordrecht, The Netherlands, 1990), Vol. 331, Chap. 13.

[29] B. Lebech, J. Bernhard, and T. Freltoft, Magnetic structures of cubic FeGe studied by small-angle neutron scattering, J. Phys.: Condens. Matter **1**, 6105 (1989).

[30] Y. Ishikawa, K. Tajima, D. Bloch, and M. Roth, Helical spin structure in manganese silicide MnSi, Solid State Commun. **19**, 525 (1976).

[31] J. Beille, J. Voiron, and M. Roth, Long period helimagnetism in the cubic B20 $Fe_xCo_{1-x}Si$ and $Co_xMn_{1-x}Si$ alloys, Solid State Commun. **47**, 399 (1983).

[32] M. Uchida, Y. Onose, Y. Matsui, and Y. Tokura, Real-space observation of helical spin order, Science **311**, 359 (2006).

[33] W. T. Jin, N. Qureshi, Z. Bukowski, Y. Xiao, S. Nandi, M. Babij, Z. Fu, Y. Su, and T. Brückel, Spiral magnetic ordering of the Eu moments in $EuNi_2As_2$, Phys. Rev. B **99**, 014425 (2019).

[34] N. S. Sangeetha, V. Smetana, A. V. Mudring, and D. C. Johnston, Helical antiferromagnetic ordering in $EuNi_{1.95}As_2$ single crystals, Phys. Rev. B **100**, 094438 (2019).

[35] M. Reehuis, W. Jeitschko, M. Möller, and P. Brown, A neutron diffraction study of the magnetic structure of $EuCo_2P_2$, J. Phys. Chem. Solids **53**, 687 (1992).

[36] N. S. Sangeetha, E. Cuervo-Reyes, A. Pandey, and D. C. Johnston, $EuCo_2P_2$: A model molecular-field helical Heisenberg antiferromagnet, Phys. Rev. B **94**, 014422 (2016).

[37] T. Nagamiya, *Helical spin ordering–1 theory of helical spin configurations*, in Solid State Physics, edited by F. Seitz, D. Turnbull, and H. Ehrenreich (Academic, New York and London, 1967), Vol. 20, p. 306.

[38] N. Higa, Q. P. Ding, F. Kubota, H. Uehara, M. Yogi, Y. Furukawa, N. Sangeetha, D. Johnston, A. Nakamura, M. Hedo *et al.*, NMR studies of the helical antiferromagnetic compound $EuCo_2P_2$, Phys. B (Amsterdam Neth.) **536**, 384 (2018).

[39] H. Kato, H. Sakai, Y. Tokiwa, S. Kambe, R. E. Walstedt, and Y. Ōnuki, Ga and Pt NMR study of $UPtGa_5$, J. Phys. Chem. Solids **63**, 1197 (2002).